Tin Nanoparticles Embedded in Carbon Buffer Layer as Preferential Nucleation Sites for Stable Sodium Metal Anodes

Journal:	*Journal of Materials Chemistry A*
Manuscript ID	TA-COM-05-2019-005176.R1
Article Type:	Communication
Date Submitted by the Author:	22-Jun-2019
Complete List of Authors:	Wang, Huan; Dartmouth College, Thayer School of Engineering Matios, Edward; Dartmouth College, Thayer School of Engineering Wang, Chuanlong; Dartmouth College, Thayer School of Engineering Luo, Jianmin; Dartmouth College, Thayer School of Engineering Lu, Xuan; Dartmouth College, Thayer School of Engineering Hu, Xiaofei; Dartmouth College, Thayer School of Engineering Zhang, Yiwen; Dartmouth College, Thayer School of Engineering Li, Weiyang; Dartmouth College, Thayer School of Engineering

Tin Nanoparticles Embedded in Carbon Buffer Layer as Preferential Nucleation Sites for Stable Sodium Metal Anodes

Huan Wang,‡ Edward Matios,‡ Chuanlong Wang,‡ Jianmin Luo, Xuan Lu, Xiaofei Hu, Yiwen Zhang and Weiyang Li*

Thayer School of Engineering, Dartmouth College, Hanover, New Hampshire 03755, United States. Email: weiyang.li@dartmouth.edu

† Electronic supplementary information (ESI) available.

‡ These authors contributed equally to this work.

Sodium (Na) metal is one of the most appealing anode materials for grid-scale energy storage systems owing to the high earth abundance and low cost of Na resources. Nevertheless, the implementation of Na metal anode is hindered by two primary issues associated with Na dendrite growth and volume expansion, resulting in low Coulombic efficiency and poor cycle life. Herein we present a facile and scalable method to synthesize tin (Sn) nanoparticles (NPs) that are uniformly embedded within carbon network (denoted as Sn@C composite), which can address the two issues simultaneously. Specifically, Sn NPs can serve as preferential nucleation sites to guide Na nucleation and thereby lower the Na deposition overpotential, while the carbon network can act as buffer layer to effectively minimize the volume change and alleviate the exfoliation of Sn NPs over repeated cycles. Consequently, high-capacity Na anodes can be realized with long-term reversibility and stability. Moreover, a room-temperature Na-sulfur battery based on the Sn@C composite as anode coupled with commercial sodium sulfide as cathode was demonstrated with significantly improved electrochemical performance. We believe this work provides a new pathway in designing high-energy Na metal batteries.

1. Introduction

Rechargeable lithium (Li)-ion batteries (LIBs) are the most widely used energy storage devices, particularly for portable electronics, smart grid and electric vehicles.[1-2] However, the increasing cost of Li resources and limited geographical distribution of Li raw materials have hindered their grid-scale applications. Just one row down from Li on the periodic table, sodium (Na) is an appealing alternative to Li because of their similar battery chemistry, high abundance of Na sources (>1000 times more abundant than Li in earth crust), and low cost of Na raw materials.[3-5] Moreover, metallic Na has high theoretical capacity (1166 mAh g^{-1}) and low electrochemical potential (-2.71 V versus standard hydrogen electrode), making it one of the most promising anode candidates.[3-5] More importantly, Na metal can be paired with a number of emerging high-capacity cathode choices, such as sulfur (S), oxygen (O_2), and carbon dioxide (CO_2). These Na-S, Na-O_2 and Na-CO_2 batteries can deliver high theoretical specific energies up to 3-4 times higher than that of the current Li-ion batteries.[6-8] Since there are generally no Na sources provided by these cathodes, Na metal is an almost exclusive anode for these high-energy ambient-temperature Na batteries.[9] However, the practical implementation of Na metal anode has been largely impeded by two fundamental challenges. First, Na metal can easily react with most organic electrolytes, leading to the formation of unstable and non-uniform solid electrolyte interphase (SEI) layer on Na metal surface that results in the rapid depletion of both electrolyte and working Na metal. Second, the relatively infinite volume change during cycling can rupture the as-formed SEI layer, leading to an increased local ion flux and dendritic Na growth. These problems cause severe electrode degradation, low Coulombic efficiency, and short circuit of the batteries.

To address these issues, there have been many proposed strategies on constructing a stable SEI layer on Na metal surface through tuning electrolyte compositions[10-19], employing a coating film,[20-26] and engineering three-dimensional (3D) hosts to cage Na metal[27-40] as well as regulating the growth behaviors of Na metal by controlling nucleation sites.[33,38-45] Among the various approaches, the infusion of molten Na metal into 3D hosts have recently attracted great interest due to the following merits: *i*) 3D hosts effectively minimize volume change via confining Na deposition within the matrix; *ii*) the Na-matrix composite improves the mechanical strength of Na metal; *iii*) high surface area host material lowers the local current density. Among them, flexible carbon-based 3D materials are the most popular hosts due to their lightweight property, chemical stability and low cost.[34-42] Meanwhile, it has been reported that the conductive nanocarbon can serve as nucleation layer to effectively decrease the energy barrier of Na plating towards long-term reversibility at a relatively low current density and capacity.[46] However, as most pristine porous carbon materials have high electronic conductivity and poor wettability with Na, the Na deposition cannot be guided into the pores of carbon hosts.[47] In this case, Na prefers to grow on the exterior of the carbon skeletons and thus forms Na agglomeration. As a result, increasing current density or capacity can result in inhomogeneous Na deposition and therefore high plating/stripping overpotential.[38-42] Recently, functional or doped carbon materials have been proposed to promote a high affinity or improved wettability between Na atom and carbon, hence contributing to homogenous Na deposition without Na dendrite growth.[37-42] Nevertheless, the introduction of functional groups or heteroatom dopants can potentially decrease the electronic conductivity of pristine carbon hosts, leading to a high resistance and large polarization at high current densities or capacities.[48] Therefore, 3D pristine carbon hosts anchored with well-distributed nanoseeds as "sodiophilic sites" to direct the Na deposition within the pores of the 3D hosts would be a desirable method to enable highly reversible and stable Na metal anodes. In addition, research in improving the long-term reversibility of high-capacity Na metal anodes using carbon matrices is still in its infancy.

Herein, we report a facile and scalable approach to synthesize tin (Sn) nanoparticles (NPs) uniformly embedded in conductive and porous carbon network (denoted as Sn@C composite). The unique structure renders high-capacity Na metal anodes with long-term reversibility and stability because of the following merits: *i*) the well-dispersed Sn NPs can provide preferential nucleation sites for Na deposition due to the alloying reaction between Na and Sn, thus lowering the Na nucleation barrier and contributing to uniform Na plating; *ii*) the conductive carbon network can serve as buffer layers to minimize the volume change and alleviate the exfoliation of Sn NPs over long-term cycles. As a result, the Sn@C composite can enable highly reversible and dendrite-free Na metal anodes with a high average Coulombic efficiency of 99.3 % at a current density of 2 mA cm^{-2} with a high capacity of 5 mAh cm^{-2} over 1250 hours. Moreover, a room-temperature Na-sulfur (S) battery based on the Sn@C composite as anode paired with commercial Na_2S powder as cathode can deliver an initial discharge capacity of 643.7 mAh g^{-1} at a current density of 1 A g^{-1} with a capacity retention of 90.5% and a high average Coulombic efficiency of 96.2% over 100 cycles.

2. Experimental section

2.1 Synthesis. The Sn@C composite was synthesized via dissolving 2 g tin (IV) chloride ($SnCl_4$, anhydrous, Alfa Aesar) and 2 g polyvinylpyrrolidone (PVP, average Mw = 55000, Sigma-Aldrich) in 100 ml methanol (anhydrous, Fisher Scientific). After 2 h of stirring, the solution was heated at 150 ^oC to obtain $SnCl_4$ wrapped in PVP polymer gel through evaporation of methanol solvent, followed by repeated evacuation and refilling in a low-pressure chemical vapor deposition system. Then the resultant solid was annealed in 300 sccm forming gas (95% argon and 5% hydrogen) at 1035 ^oC for 6 h. Overall, $SnCl_4$ can be uniformly trapped in PVP gel network by stirring, which is in-situ reduced to metallic Sn NPs at high temperature while PVP is simultaneously carbonized, leading to the formation of Sn NPs homogenously embedded into the conductive carbon network. The synthesis of pure carbon network was through a similar process without the presence of $SnCl_4$. For the synthesis of bare Sn nanoparticles, metallic Sn with a thickness of 10 nm was thermally evaporated onto Cu substrate followed by annealing at 250 ^oC for 1 h in 100 sccm forming gas.

2.2 Characterization: Scanning electron microscope (SEM) and energy dispersive spectroscopy (EDS) images were performed on a FEI Scios2 SEM with EDS imaging. Transmission electron microscope (TEM) imaging was obtained using a FEI Tecnai F20 TEM equipment operating at 200 kV. Raman spectra were collected on a Horiba HR800 Raman system with 532 nm excitation. X-ray diffraction (XRD) measurements were conducted on Rigaku (model #007) X-ray diffractometer equipped with a Cu-target X-ray tube (λ=0.154 nm) operated at 300 mA and 40 kV. Thermogravimetric analysis (TGA) was carried out on a Pyris Diamond Thermogravimetric/Differential Thermal Analyzer (PerkinElmer Instruments) from room temperature to 680 ^oC at a heating rate of 5 ^oC min^{-1} in air.

2.3 Electrode preparation: The working electrodes were composed of active materials and polyvinylidene fluoride (PVDF) based on a mass ratio of 9:1, which was then dispersed in N-methyl-2-pyrrolidinone (NMP, average Mw = 55000, Sigma-Aldrich) to form a homogenous slurry. The as-obtained slurry was casted onto Cu foil (25 μm thick, Alfa Aesar) and dried at 80 ^oC overnight in a vacuum oven. The typical mass loading of active material was 1-1.2 mg cm^{-2}. For the fabrication of full cell, commercial sodium sulfide (Na_2S, anhydrous granular, Alfa Aesar) chunks were ground into fine powders in an Argon-filled glove box (Mbraun, H_2O <0.1, O_2 <

0.6). Then the Na_2S powder was mixed with super P carbon black (TIMCAL Ltd, C·NERGY™ SUPER C65) and PVDF following a weight ratio of 6:3:1 in NMP solvent under overnight stirring to form a homogenous slurry. Then the as-obtained slurry was casted onto carbon fiber paper (fuel cell store) and dried at 80 °C overnight. The average mass loading of Na_2S is around 1.2 mg cm^{-2}.

2.4 Electrochemical Measurements: The electrochemical Na plating/stripping process was conducted in 2032-type coin cells with Na disk as counter and reference electrode in the Argon-filled glove box. 1 M sodium hexafluorophorophosphate ($NaPF_6$, 99%, Alfa Aesar) in diethylene glycol dimethyl ether (diglyme, anhydrous, Sigma-Aldrich) was employed as electrolyte. The reversibility test was evaluated via LAND tester under galvanostatic conditions. A constant current with a constant capacity (the amount of Na deposited) was applied to the electrode, followed by Na stripping via charging to 1 V (versus Na^+/Na). For the full cell, the electrolyte consisted of 1 M $NaPF_6$ in diglyme and 1,3-dioxolane (DOL, anhydrous, Sigma-Aldrich) (1:1 by volume) with 0.049 M of both Na_2S and phosphorous pentasulfide as additives. The assembled full cells were galvanically charged and discharged using standard testing system within voltage range from 1.0 V to 2.6 V. The cyclic voltammetry (CV) curve was measured on an electrochemical workstation (VMP3, Bio-Logic Science Instruments) at a scan rate of 0.2 mV s^{-1}.

3. Results and discussion.

The Sn@C composite was synthesized through a dissolution-precipitation of $SnCl_4$ with the assistance of PVP followed by carbonization in reducing atmosphere, leading to Sn NPs being homogenously embedded within the conductive carbon network. The morphology of the as-prepared Sn@C composite was revealed by SEM and TEM characterization. As shown in Fig. 1a, b, embedded Sn NPs within the carbon matrix can be visually confirmed by the SEM images. The average diameter of Sn NPs is around 150 nm, which can be clearly observed from high-magnification SEM and TEM images, respectively (Fig. 1c, d). The uniform distribution of Sn NPs can be further revealed by EDS mapping of elemental Sn (Fig. S1). High-resolution TEM imaging shows that Sn NP are uniformly wrapped with a thin carbon layer with a shell thickness of around 5 nm (Fig. 1e). We believe this uniform coating can effectively prevent particle aggregation and alleviate the exfoliation of Sn NPs during repeated sodiation/desodiation process. The lattice fringe exhibits an interplanar spacing of 0.291 nm, which matches well with (200) plane of metallic Sn, thereby confirming the high crystallinity of the as-obtained Sn@C composite. Based on the TGA curve (Fig. S2), the Sn content in Sn@C composite was calculated to be around 5.6 wt%,[49] which reveals that the mass ratio of Sn to C was relatively low (~1:19), indicating that the as-prepared Sn@C composite can preserve the lightweight character of carbon matrix.

Raman spectrum of Sn@C composite in Fig. 1f presents two characteristic peaks of D band (~1340.6 cm^{-1}) and G band (~1580 cm^{-1}), corresponding to A_{1g} breathing-mode vibration of C_6 rings and E_{2g} vibration mode of sp^2 bonded carbon, respectively.[50] The higher intensity of G band relative to that of D band indicates that the carbon matrix has a high degree of graphitization, thus possessing high electronic conductivity,[51-53] which can facilitate electron transport and reduce the polarization. All peaks in the XRD profile of Sn@C composite powder (Fig. 1g) are assigned to metallic Sn (PDF #65-2631). After sodiation, new peaks associated with $Na_{15}Sn_4$ (PDF #31-1327) can be detected due to the alloying reaction between metallic Sn and Na,[54] accompanied with the appearance of new peaks corresponding to metallic Na.

The plating/stripping reversibility of Na metal electrodes was investigated using a two-electrode configuration composed of metallic Na electrode and Cu foil coated by Sn@C composite (substrate for Na plating/stripping). The Coulombic efficiency of each cycle is calculated as the ratio of stripped Na (based on capacity extracted) over plated Na (based on capacity deposited) onto the substrate of Sn@C composite. Meanwhile, to confirm the synergetic effect of Sn NPs and carbon matrix are both the critical factors for enabling reversible and stable Na metal electrodes, control experiments with bare Cu foil, bare Sn nanoparticles (Fig. S3) and pure carbon matrix (Fig. S4) were also employed as the substrates for Na plating/stripping tests. At a current density of 2 mA cm^{-2} and a capacity of 1 mAh cm^{-2}, the Sn@C composite electrode exhibits an extremely high and consistent average Coulombic efficiency of ~99.7% with the smallest voltage hysteresis of ~30 mV over 500 cycles (Fig. 2a, d). In contrast, the Coulombic efficiency and voltage hysteresis for bare Cu foil are both highly fluctuated, possibly due to the repeated growth/dissolution of Na dendrites over cycling. Moreover, pure carbon matrix also shows a low Coulombic efficiency with high fluctuation (Fig. S5) under the same cycling condition, suggesting that Na preferentially deposits on the surface of the conductive carbon matrix, rather than into the channels due to the lack of preferential nucleation sites, which will be discussed in detail later. As for bare Sn nanoparticles, the Coulombic efficiency rapidly dropped to below 80% after just 50 cycles and the cell short circuited after 150 cycles (Fig. 2a, d), which can be caused by the exfoliation of Sn nanoparticles due to volume expansion during repeated sodiation/desodiation.[55] Moreover, the Na nucleation barrier (defined as the difference between the flat plateau and the bottom of the voltage dip) on Sn@C composite is much smaller than that on pure carbon matrix (Fig. S6), confirming that the well-dispersed Sn NPs can act as nanoseeds to lower the nucleation overpotential for uniform Na deposition.[47] Meanwhile, the stripping-plating voltage profiles on the above four kinds of substrates at various cycles are shown in Fig. S7. The capacity loss on Sn@C composite is inconspicuous and the charging-discharging curves from the 1st cycle to the 500th cycle almost completely overlap, indicating the high reversibility of Na stripping and plating. However, for the substrates of bare Sn nanoparticles and bare Cu foil, cell short circuit results in charging failure at the 144th and the 162nd cycle, respectively. As to pure carbon network, large amounts of irreversible capacity loss can be observed with high voltage hysteresis. In addition, the Sn@C composite exhibits an anodic peak at a lower potential compared to bare Sn nanoparticles and bare Cu foil in the CV curves (Fig. S8), which further suggests the good kinetics of Na stripping and plating on Sn@C composite.[10]

As the capacity is increased to 3 mAh cm^{-2}, the Sn@C composite electrode can still maintain a high average Coulombic efficiency of ~99.5% with the highest stability in voltage hysteresis over 250 cycles (Fig. 2b, e). In comparison, the bare Cu foil electrode exhibits an even more unstable and low Coulombic efficiency with highly varied voltage hysteresis. Meanwhile, the Coulombic efficiency for the case of bare Sn nanoparticles rapidly decay to 50% in just 50 cycles and finally short circuited after 75 cycles. Impressively, at an even higher capacity of 5 mAh cm^{-2}, the Coulombic efficiency for Sn@C composite can still be stabilized at ~99.3% with the lowest voltage hysteresis of ~30 mV over 250 cycles (1250 hours) (Fig. 2c, f), proving its outstanding reversibility and high Na utilization as a high-capacity Na metal electrode. Notably, compared to the other three kinds of plating substrates (bare Cu foil, bare Sn nanoparticles and pure carbon matrix), the Sn@C composite can deliver a consistently low voltage hysteresis and stable voltage profile as well as constantly low nucleation barrier over repeated plating/stripping process at different capacities (Fig. 2d-f, Fig. S9 and S10). This phenomenon can be attributed to the presence of abundant Sn nanoparticles uniformly embedded within the carbon network, thereby providing ample Na nucleation sites to guide the homogenous Na plating on the Sn@C composite electrode. Moreover, the Na nucleation for subsequent deposition preferentially occurs on the as-formed Na_4Sn_{15} alloy sites, rather than on the carbon surface, thus lowering the nucleation barrier for Na deposition and consequently contributing to uniform Na plating.

The schematic of Na nucleation and growth on the Sn@C composite electrode is illustrated in Fig. 3a, which is further confirmed by ex-situ SEM characterization at a current density of 2 mA cm^{-2} with different plating capacities. At an initial capacity of 1 mAh cm^{-2}, it can be observed that Na deposits into the carbon network and preferentially reacts with embedded Sn nanoparticles followed by subsequent nucleation around the as-formed alloy, exhibiting island growth mode within the interlayer of carbon network (Fig. 3b, e). With an increased plating capacity of 3 mAh cm^{-2}, the small Na islands gradually merge into larger island on each piece of carbon matrix with flat surface morphology (Fig. 3c, f). Subsequently, as the capacity is increased to 5 mAh cm^{-2}, the deposited Na gradually fills the gaps of carbon matrix and exhibits a smooth surface without Na dendrite growth (Fig. 3d, g). After 50 cycles of deposition at a current density of 2 mA cm^{-2} and a capacity of 1 mAh cm^{-2}, it can be clearly observed that Sn@C composite electrode remains to be free of Na dendrites (Fig. 3h). In comparison, bare Sn nanoparticles are covered by non-continuous Na deposits (Fig. 3i). For the bare Cu foil, obvious Na dendrites can be observed on the surface (Fig. 3j). As to pure carbon matrix, the surface shows high density of mossy/dendritic Na structures (Fig. S11), indicating that it is difficult for Na^+ ions to deposit into the gaps of carbon matrix without the presence of the nucleation sites. The above results confirm that the Sn@C composite can provide plentiful "hot spots" (Sn NPs) with enhanced binding affinity with Na atoms via the alloying process and meanwhile confine the Na nucleation/growth within the buffer carbon matrix, promoting uniform Na plating without dendrite formation.

To further evaluate the electrochemical performance of Sn@C composite as Na anode, room-temperature Na-S batteries were assembled to demonstrate its superiority of highly reversible Na plating/stripping. It is worth mentioning that compared to elemental S cathode for Na-S batteries, Na_2S is a more desirable starting cathode material because it is in fully sodiated state (potentially being coupled with Na-metal-free anode) and can alleviate the large volume expansion of S cathode (Na_2S is already at the expanded state).[56,57] Based on these considerations, we employed commercial Na_2S powder with an average size of ~2-5 μm as cathode material (Fig. S12) and Sn@C composite pre-deposited with 1 mAh cm^{-2} of Na (denoted as Sn@C composite/Na) as anode material, respectively. For comparison, bare Na metal, bare Sn nanoparticles pre-deposited with 1 mAh cm^{-2} of Na (denoted as Sn/Na), and bare Cu foil pre-deposited with 1 mAh cm^{-2} of Na (denoted as Cu/Na) were also used, respectively, as anode materials to pair with the commercial Na_2S powder cathode. All capacities are calculated based on the active mass loading of S. As shown in Fig. 4a, the Na-S full cell with Sn@C composite/Na anode exhibits a far more superior electrochemical performance compared to the cells using bare Na metal anode and Cu/Na anode, showing an initial discharge capacity of 643.7 mAh g^{-1} at a current density of 1 A g^{-1}. After 100 cycles, the reversible capacity can still be stabilized at 582.3 mAh g^{-1}, corresponding to a high capacity retention of 90.5%. Moreover, the Na^+ ions tend to deposit on the as-formed Na_4Sn_{15} alloy within the carbon matrix, which can effectively alleviate the shuttle effect, leading to a high average Coulombic efficiency of ~96.2% over 100 cycles. In contrast, the Na-S full cell using bare Na metal anode delivers an unstable Coulombic efficiency and rapidly decayed discharge capacity, especially in the first 20 cycles. Ultralow capacity with unsatisfactory Coulombic efficiency was also observed for the case of bare Cu/Na anode. For the Na-S full cell with bare Sn/Na as anode, the discharge capacity rapidly decays to below 100 mAh g^{-1} in the first 20 cycles with an average Coulombic efficiency of ~70% and finally dropped to almost zero after 60 cycles (Fig. S13). These results suggest that the Sn@C composite has a significant contribution to reversible and stable Na-S batteries.

Fig. 4b shows the corresponding charge-discharge voltage profiles for Na-S full cell using Sn@C composite/Na anode at different cycles within the voltage range of 1-2.6 V at 1 A g^{-1}. During the discharging process, the first voltage plateau at ~2.10 V and the voltage slope in the range of 2.10 V-1.55 V correspond to the conversions from S_8 to long-chain soluble sodium polysulfides (Na_2S_x, x=4-8). The second voltage plateau at ~1.55 V and the voltage slope in the range of ~1.55 V-1.0 V can be assigned to the transition to the insoluble short-chain solid sodium polysulfides (Na_2S_x, x=1-3). During the charging process, two potential plateaus at ~1.75 V and ~2.24 V as well as two potential slopes can also be observed at different cycles, which is attributed to the reverse reactions in the oxidation process. This is in good agreement with the corresponding CV profile shown in Fig. S14, in which the charging and discharging curve both display two obvious peaks. In comparison, no peaks corresponding to the conversion from long-chain soluble Na_2S_x (x=4-8) to insoluble short-chain Na_2S_x (x=1-3) can be observed in the CV curves of Na-S full cells using Cu/Na or Sn/Na anode. This could be caused by the irreversibility of anode and severe shuttle effect in the absence of carbon matrix. The nearly overlapping voltage vs. specific capacity curves of the 1st cycle to the 50th cycle suggest the high reversibility of the Na-S full cell enabled by Sn@C composite/Na anode. Additionally, the Na-S full cell with Sn@C composite/Na as anode also exhibits dramatically improved rate capabilities compared with that using bare Na metal anode (Fig. 4c). It is noted that the cycling stability and rate capability of the full cell using Sn@C composite/Na as anode and commercial Na_2S powder as cathode is competitive among the reported works on room-temperature Na-S batteries (Table S1), in which efforts are mainly dedicated to elaborate nanomaterial design for cathode.[56-69] Overall, these results coherently demonstrate the significant improvement in the electrochemical performance of the full cell using Sn@C composite/Na anode.

4. Conclusions

In summary, we have successfully synthesized Sn nanoparticles homogeneously embedded in conductive carbon network, enabling highly reversible and stable Na anodes through the following two aspects. First, the Sn nanoparticles can provide abundant nucleation sites to lower the nucleation barrier for Na growth. Second, the carbon network can act as buffer layer to alleviate the volume change. Consequently, the Sn@C composite can deliver an extremely stable and reversible Na plating/stripping behavior at a current density of 2 mA cm^{-2} and a high capacity of 5 mAh cm^{-2} with a nearly 100% of Coulombic efficiency and a consistently low voltage hysteresis of ~30 mV over 1250 hours. Meanwhile, a room-temperature Na-S battery based on the Sn@C composite as anode and commercial Na_2S as cathode shows dramatically improved electrochemical performance with an initial discharge capacity of 643.7 mAh g^{-1} and a high capacity retention of 90.5% at 1 A g^{-1} after 100 cycles as well as an average Coulombic efficiency of 96.2%. We believe this work provides a cost-effective method in developing high-performance Na metal batteries.

Conflicts of interest

There are no conflicts of interest to declare.

Acknowledgements

The authors greatly acknowledge the support from Young Investigator Program funded by U.S. Air Force Office of Scientific Research under award FA9550-17-1-0184 and support from the start-up funds at Thayer School of Engineering, Dartmouth College.

References

1. A. Yoshino, *Angew. Chem. Int. Ed.* 2012, **51**, 5798-5800.
2. J. B. Goodenough and K-S Park, *J. Am. Chem. Soc.* 2013, **135**, 1167-1176.
3. B. Lee, E. Paek, D. Mitlin and S. W. Lee, *Chem. Rev.* 2019, **119**, 5416−5460.
4. Y. Zhao, K. R. Adair and X. Sun. *Energy Environ. Sci.*, 2018, **11**, 2673-2695.
5. C. Zhao, Y. Lu, J. Yue, D. Pan, Y. Qi, Y-S Hu and L. Chen, *J Energy Chem*., 2018, **27**, 1584-1596.
6. Y-X. Wang, B. Zhang, W. Lai, Y. Xu, S-L. Chou, H-K. Liu and S-X. Dou, *Adv. Energy Mater.* 2017, **7**, 1602829;
7. P. Hartmann, C. L. Bender, M. Vracar, A. K. Durr, A. Garsuch, J. Janek and P. Adelhelm, *Nat. Mater.* 2013, **12**, 228-232.
8. X. Hu, J. Sun, Z. Li, Q. Zhao, C. Chen and J. Chen, *Angew. Chem. Int. Ed.* 2016, **55**, 6482-6486.
9. W. Luo, F. Shen, C. Bommier, H. Zhu, X. Ji and L. Hu, *ACC. Chem. Res.* 2016, **49**, 231.
10. Z. W. Seh, J. Sun, Y. Sun and Y. Cui, *ACS Cent. Sci.* 2015, **1**, 449-455.
11. J. Song, G. Jeong, A-J. Lee, J. H. Park, H. Kim and Y-J. Kim, *ACS Appl. Mater. Interfaces* 2015, **7**, 27206−27214.
12. R. Cao, K. Mishra, X. Li, J. Qian, M. H. Engelhard, M. E. Bowden, K. Han, K. T. Mueller, W. A. Henderson and J-G. Zhang, *Nano Energy* 2016, **30**, 825-830.
13. J. Lee, Y. Lee, J. Lee, S. M. Lee, J. H. Choi, H. Kim, M. S. Kwon, K. Kang, K. T. Lee and N. S. Choi, *ACS Appl. Mater. Interfaces* 2017, **9**, 3723-3732.
14. H. Wang, C. Wang, E. Matios and W. Li, *Angew. Chem., Int. Ed.* 2018, **57,** 7734-7737.
15. Q. Shi, Y. Zhong, M. Wu, H. Wang and H. Wang, *Angew. Chem. Int. Ed.* 2018, **130**, 9207-9210.
16. J. Zheng, S. Chen, W. Zhao, J. Zhao, J. Song, M. H. Engelhard and J-G Zhang, *ACS Energy Lett.* 2018, **3**, 315-321.

17. L. Lutz, D. A. Dalla Corte, M. Tang, E. Salager, M. Deschamps, A. Grimaud, L. Johnson, P. G. Bruce and J-M. Tarascon, *Chem. Mater*. 2017, **29**, 6066-6075.

18. S. Wei, S. Choudhury, J. Xu, P. Nath, T. Tu and L. A. Archer, *Adv. Mater.* 2017, **29**, 1605512.

19. D. Ruiz-Martinez, A. Kovacs and R. Gómez, *Energy Environ. Sci.,* 2017, **10,** 1936-1941.

20. H. Wang, C. Wang, E. Matios and W. Li, *Nano Lett.* 2017, **17**, 6808-6815.

21. Y. Zhao, L. V. Goncharova, A. Lushington, Q. Sun, H. Yadegari, B. Wang, W. Xiao, R. Li and X. Sun, *Adv. Mater.* 2017, **29**, 1606663.

22. W. Luo, C. Lin, O. Zhao, M. Noked, Y. Zhang, G. W. Rubloff and L. Hu, *Adv. Energy Mater.* 2017, **7**, 1601526.

23. Y. J. Kim, H. Lee, H. Noh, J. Lee, S. Kim, M. H. Ryou, Y. M. Lee and H. T. Kim, *ACS Appl. Mater. Interfaces*, 2017, **9**, 6000-6006.

24. S. Choudhury, S. Wei, Y. Ozhabes, D. Gunceler, M. J. Zachman, Z. Tu, J. H. Shin, P. Nath, A. Agrawal, L. F. Kourkoutis, T. A. Arias and L. A. Archer, *Nat. Commun.* 2017, **8**, 898.

25. Y. Zhao, L. V. Goncharova, Q. Zhang, P. Kaghazchi, Q. Sun, A. Lushington, B. Wang, R. Li and X. Sun, *Nano Lett.* 2017, **17**, 5653-5659.

26. Z. Xu, J. Yang, T. Zhang, L. Sun, Y. Nuli, J. Wang and S-i. Hirano, *Adv. Funct. Mater*. 2019, 1901924. DOI: 10.1002/adfm.201901924.

27. S. Liu, S. Tang, X. Zhang, A. Wang, Q. Yang and J. Luo, *Nano Lett.* 2017, **17**, 5862-5868.

28. C. Wang, H. Wang, E. Matios, X. Hu and W. Li, *Adv. Funct. Mater.* 2018, **28**, 1802282.

29. J. Luo, C. Wang, H. Wang, X. Hu, E. Matios, X. Lu, W. Zhang, X. Tao and Li. W. *Adv. Funct. Mater*. 2019, **29**, 1805946.

30. H. Ye. C-Y. Wang, T-T. Zuo, P-F. Wang, Y-X Yin, Z-J. Zheng, P. Wang, J. Cheng, F-F. Cao and Y-G. Guo, *Nano Energy* 2018, **48**, 369-376.

31. Q. Zhang, Y. Lu, M. Zhou, J. Liang, Z. Tao and J. Chen, *Inorg. Chem. Front.,* 2018, **5**, 864-869.

32. Z. Wang, X. Zhang, S. Zhou, K. Edström, M. Strømme and L. Nyholm, *Adv. Funct. Mater.* 2018, **28**, 1804038.

33. M. Zhu, S. Li, B. Li, Y. Gong, Z. Du and S. Yang, *Sci. Adv.* 2019, **5**, eaau6264.

34. S. Chi, X. Qi, Y. Hu, L and Z. Fan, *Adv. Energy Mater.* 2018, **8**, 1702764.

35. W. Luo, Y. Zhang, S. Xu, J. Dai, E. Hitz, Y. Li, C. Yang, C. Chen, B. Liu and L. Hu, *Nano Lett.* 2017, **17**, 3792-3797.

36. H. J. Yoon, N. R. Kim, H-J. Jin and Y. Yun, *Adv. Energy Mater.* 2017, **7**, 1701261.

37. A. Wang, X. Hu, H. Tang, C. Zhang, S. Liu, Y. Yang, Q-H. Yang and J. Luo, *Angew. Chem. Int. Ed.* 2017, **56**, 11921-11926.

38. Z. Wang, M. Li, C. Ruan, C, Liu, C. Zhang, C. Xu, K. Edström, M. Strømme and L. Nyholm, *J. Phys. Chem. C* 2018, **22**, 23352-23363.

39. Y. Zhao, X. Yang, L-Y. Kuo, P. Kaghazchi, Q. Sun, J. Liang, B. Wang, A. Lushington, R. Li, H. Zhang and X. Sun, *Small* 2018, **14**, 1703717.

40. Z. Zheng, X. Zeng, H. Ye, F. Cao and Z. Wang, *ACS Appl. Mater. Interfaces* 2018, **10**, 30417-30425.

41. B. Sun, P. Li, J. Zhang, D. Wang, P. Munroe, C. Wang, P. H. L. Notten and G. Wang. *Adv. Mater.* 2018, **30**, 1801334.

42. X. Hu, P. H. Joo, H. Wang, E. Matios, C. Wang, J. Luo, X. Lu, K. Yang and W. Li, *Adv. Funct. Mater.* 2019, **29**, 1807974.

43. S. Tang, Z. Qiu, X-Y. Wang, Y. Gu, X-G. Zhang, W-W. Wang, J-W. Yan, M-S. Zheng, Q-F. Dong and B-W. Mao, *Nano Energy* 2018, **48**, 101-106.

44. S. Tang, X-Y. Zhang, X-G. Zhang, J-T. Li, X-Y. Wang, J-W. Yan, D-Y. Wu, M-S. Zheng, Q-F. Dong and B-W. Mao, *Adv. Mater.* 2019, **31**, 1807495.

45. J. Jung, D. Y. Hwang, I. Kristanto, S. K. Kwak and S. J. Kang, *J. Mater. Chem. A,* 2019, **7**, 9773.

46. A. P. Cohn, N. Muralidharan, R. Carter, K. Share and C. L. Pint, *Nano Lett.* 2017, **17**, 1296-1301.

47. K. Yan, Z. Lu, H-W, Lee, F. Xiong, P-C, Hsu, Y. Li, J. Zhao, S. Chu and Y. Cui, *Nat. Energy* 2016, **1**, 16010.

48. R. Zhang, X-B. Cheng, C-Z. Zhao, H-J, Peng, J-L, Shi, J-Q, Huang, J. Wang, F. Wei and Q. Zhang, *Adv. Mater.* 2016, **28**, 2155-2162.

49. Z. Zhu, S. Wang, J. Du, Q. Jin, T. Zhang, F. Cheng and J. Chen, *Nano Lett.* 2014, **14**, 153-157.

50. X. Hu, X. Sun, S. J. Yoo, B. Evanko, F. Fan, S. Cai, C. Zheng, W. Hu and G. D. Stucky, *Nano Energy* 2019, **56**, 828-839.

51. S. Gupta, B. R. Weiner and G. Morrell. *J. Appl. Phys.* 2002, **92**, 5457-5462.

52. N. Amini, K-F. Aguey-Zinsou and Z-X. Guo. *Carbon*, 2011, **49**, 3857-3864.

53. I. K. Moon, J. Lee, R. S. Ruoff and H. Lee. *Nat. Commun.* 2010, **1**, 73.

54. L. D. Ellis, T. D. Hatchard and M. N. Obrovac. *J. Electrochem. Soc.* 2012, **159**, A1801-A1805.

55. H. Ying and W-Q. Han, *Adv. Sci.* 2017, **4**, 1700298.

56. C. Wang, H. Wang, X. Hu, E. Matios, J. Luo, Y. Zhang, X. Lu and W. Li, *Adv. Energy Mater.* 2019, **9,** 1803251.

57. X. Yu and A. Manthiram. *Chem. Mater.* 2016, **28,** 896-905.

58. S. Zheng, P. Han, Z. Han, P. Li, H. Zhang and J. Yang. *Adv. Energy Mater*. 2014, **4**, 1400226.

59. X. Yu and A. Manthiram. *Chem. Eur. J.* 2015, **21**, 4233-4237.

60. X. Yu and A. Manthiram. *Adv. Energy Mater.* 2015, **5**, 1500350.

61. S. Wei, S. Xu, A. Agrawral, S. Choudhury, Y. Lu, Z. Tu, L. Ma and L. A. Archer. *Nat. Commun*. 2016, **7**, 11722.

62. B-W. Zhang, T. Sheng, Y-X. Wang, S. Chou, K. Davey, S-X. Dou and S-Z. Qiao, *Angew. Chem. Int. Ed.* 2019, **58**, 1484-1488.

63. Y-M. Chen, W. Liang, S. Li, F. Zou, S. M. Bhaway, Z. Qiang, M. Gao, B. D. Vogt and Y. Zhu. *J. Mater. Chem. A*, 2016, **4**, 12471-12478.

64. D. Ma, Y. Li, J. Yang, H. Mi, S. Luo, L. Deng, C. Yan, M. Rauf, P. Zhang, X. Sun, X. Ren, J. Li and H. Zhang. *Adv. Funct. Mater.* 2018, **28**, 1705537.

65. X. Xu, D. Zhou, X. Qin, K. Lin, F. Kang, B. Li, D. Shanmukaraj, T. Rogo, M. Armand and G. Wang. *Nat. Commun.* 2018, **9**, 3870.

66. B-W. Zhang, T. Sheng, Y-D. Liu, Y-X. Wang, L. Zhang, W-H. Lai, L. Wang, J. Yang, Q-F. Gu, S-L. Chou, H-K. Liu and S-X. Dou, *Nat. Commun.* 2018, **9**, 4082.

67. R. Carter, L. Oakes, A. Douglas, N. Muralidharan, A. P. Cohn and C. L. Pint. *Nano Lett.* 2017, **17**, 1863-1869.

68. T. H. Hwang, D. S. Jung, J-S. Kim, B. G. Kim and J. W. Choi. *Nano Lett.* 2013, **13**, 4532-4538.

69. M. Kohl, F. Borrmann, H. Althues and S. Kaskel. *Adv. Energy Mater*. 2016, **6**, 1502185.

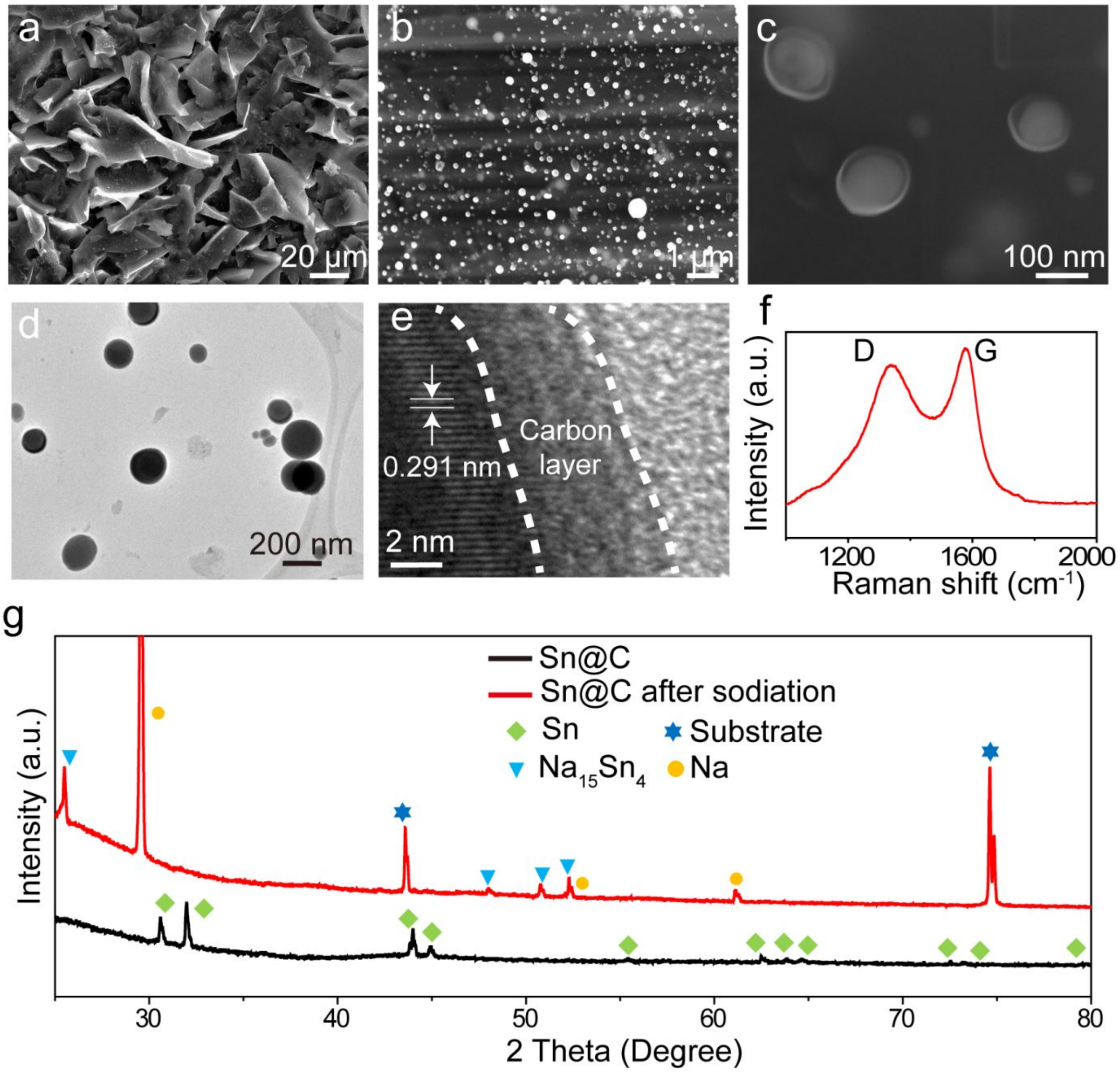

Fig. 1 Characterization of Sn@C composite. (a-c) SEM images at different magnifications; (d) Low-magnification and (e) high-resolution TEM images; (f) Raman spectrum; (g) XRD profiles before and after sodiation on stainless steel as substrate. White dashed lines in (e) indicate the boundary of carbon layer.

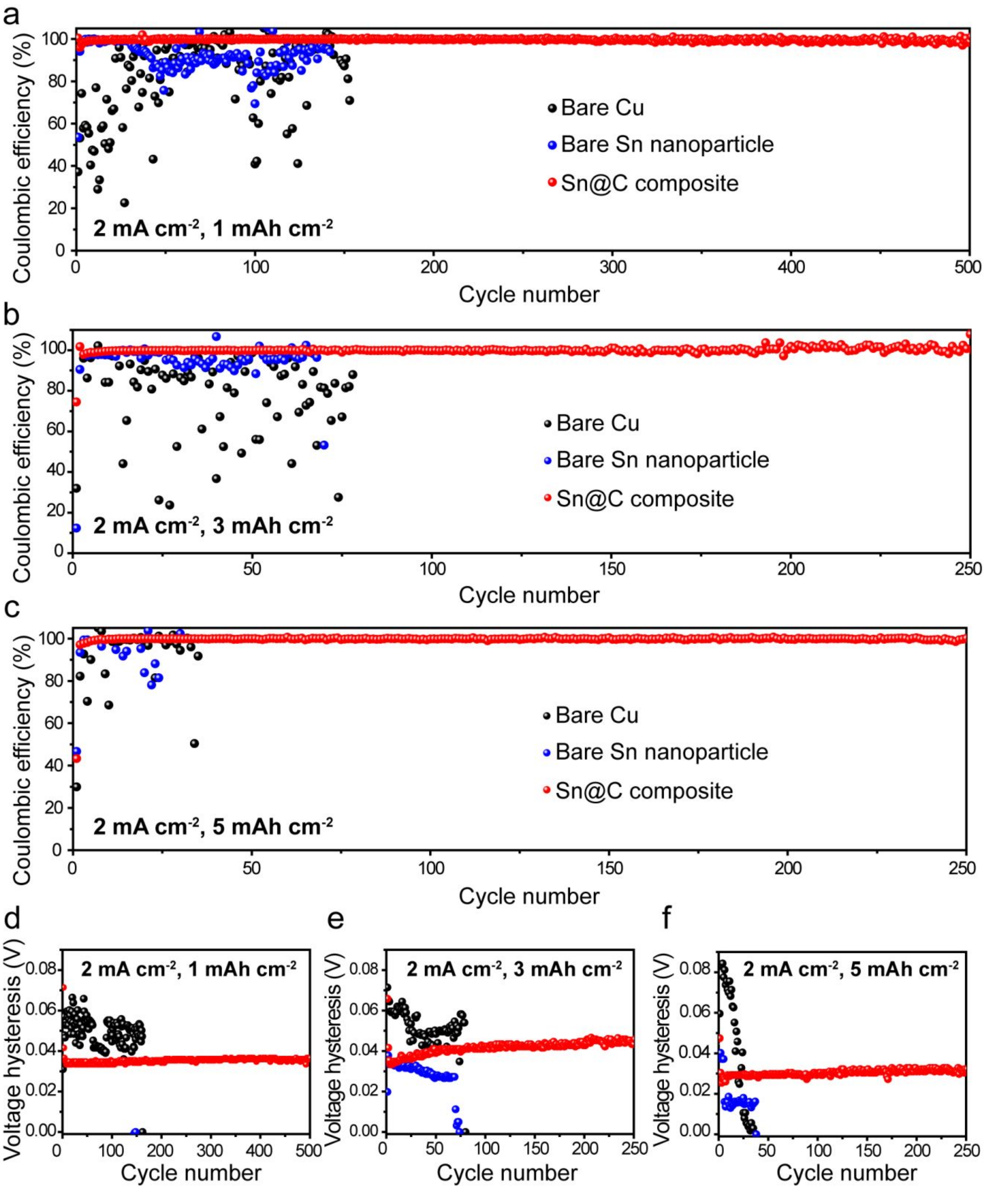

Fig. 2 Coulombic efficiencies of Na plating on different substrates at a current density and capacity of (a) 2 mA cm^{-2}, 1 mAh cm^{-2}; (b) 2 mA cm^{-2}, 3 mAh cm^{-2}; (c) 2 mA cm^{-2}, 5 mAh cm^{-2}. (c-d) Corresponding voltage hysteresis versus cycles.

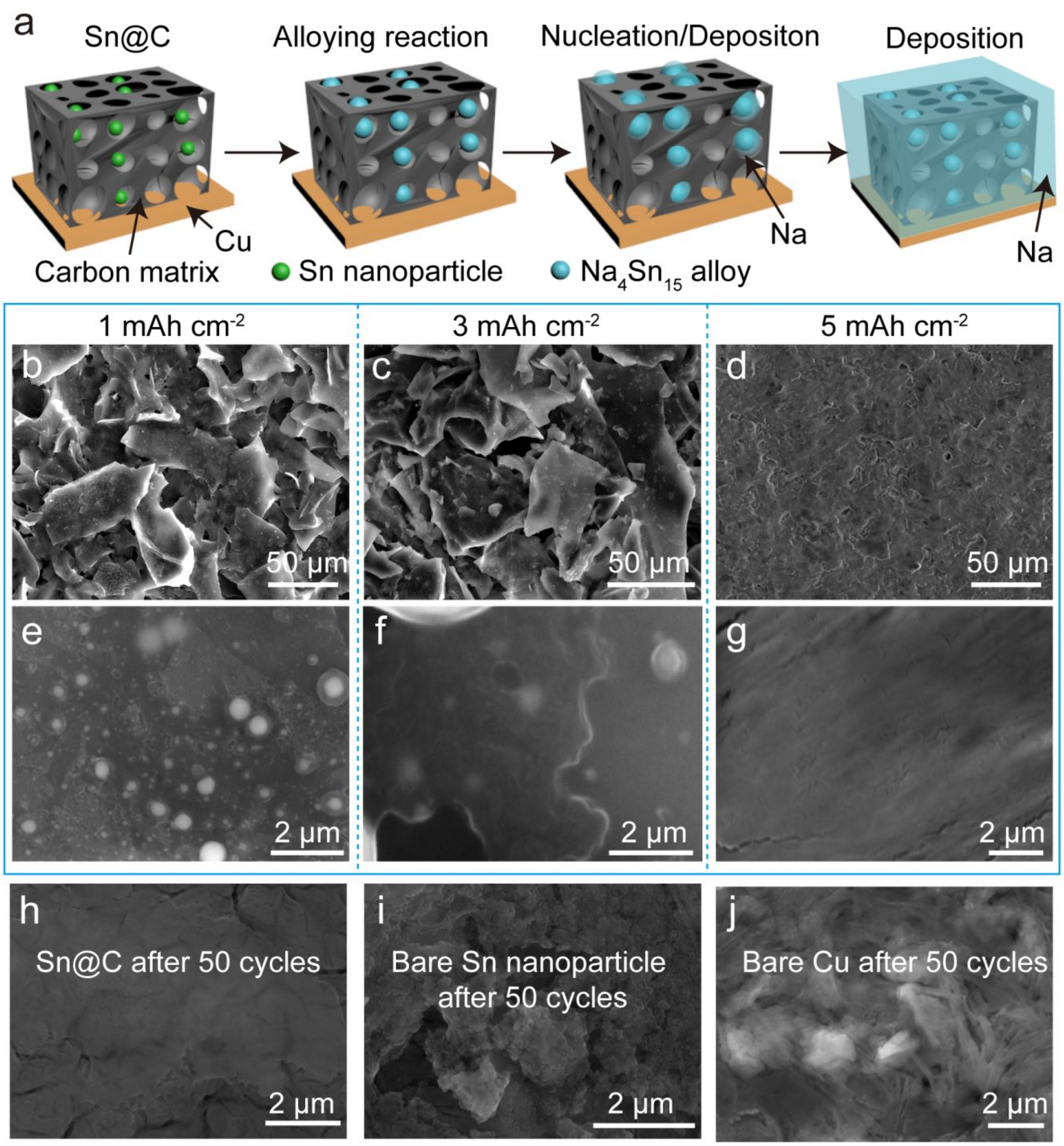

Fig. 3 (a) Schematic diagrams of Na nucleation and growth behavior on the substrate of Sn@C composite. SEM images of the surface morphologies of Sn@C composite at a current density of 2 mA cm^{-2} and a capacity of (b, e) 1 mAh cm^{-2}; (c, f) 3 mAh cm^{-2}; (d, g) 5 mAh cm^{-2}. Images in (b, c, d) and (e, f, g) are at low and high magnifications, respectively. SEM images of Na cycling at a current density 2 mA cm^{-2} and a capacity of 1 mAh cm^{-2} after the 50th cycle of deposition on (h) Sn@C composite; (i) bare Sn nanoparticle; (j) bare Cu foil.

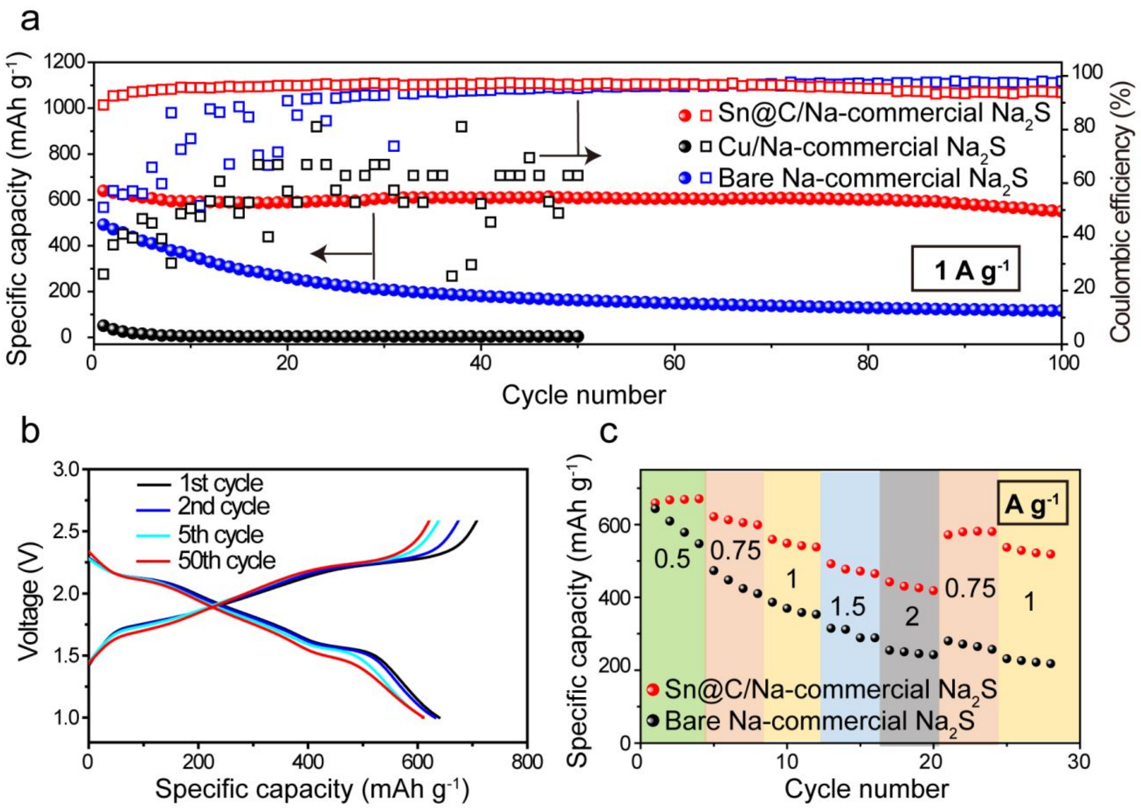

Fig. 4 (a) Cycling performance and Coulombic efficiencies of Na-S full cells using commercial Na_2S powder as cathode with three kinds of anodes (Sn@C/Na, Cu/Na and bare Na), respectively, at 1 A g^{-1} in the potential range of 1-2.6 V. (b) Charge-discharge voltage profiles of the cell with the Sn@C composite/Na anode at the 1st, 2nd, 5th and 50th cycle at 1 A g^{-1}. (c) Rate capabilities of the Na-S full cells using Sn@C composite/Na and bare Na anode discharged at various current rates, respectively.

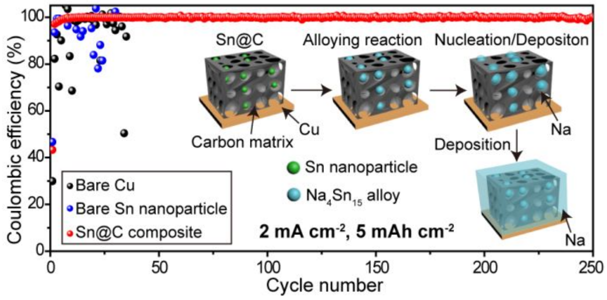

High-capacity sodium anodes with long-term reversibility and stability are presented by synthesizing tin nanoparticles homogeneously embedded within conductive carbon network.